

# Flow Shadowing: A Method to Detect Multiple Flow Headings using an Array of Densely Packed Whisker-inspired Sensors

Teresa A. Kent<sup>1</sup> and Sarah Bergbreiter<sup>2</sup>

**Abstract**—Understanding airflow around a drone is critical for performing advanced maneuvers while maintaining flight stability. Recent research has worked to understand this flow by employing 2D and 3D flow sensors to measure flow from a single source like wind or the drone’s relative motion. Our current work advances flow detection by introducing a strategy to distinguish between two flow sources applied simultaneously from different directions. By densely packing an array of flow sensors (or whiskers), we alter the path of airflow as it moves through the array. We have named this technique “flow shadowing” because we take advantage of the fact that a downstream whisker shadowed (or occluded) by an upstream whisker receives less incident flow. We show that this relationship is predictable for two whiskers based on the percent of occlusion. We then show that a 2x2 spatial array of whiskers responds asymmetrically when multiple flow sources from different headings are applied to the array. This asymmetry is direction-dependent, allowing us to predict the headings of flow from two different sources, like wind and a drone’s relative motion.

## I. INTRODUCTION

Direct measurement of airflow around a drone (e.g., the velocity and direction of flow) has led to several improvements in drone flight control [1], [2], [3]. Most drones experience at least two sources of airflow: 1) the relative motion of the drone and 2) environmental sources, such as wind. Direct measurement of drone velocity through airflow can provide real-time feedback and improved state estimation [3], [4], [5]. Measurement of environmental wind flow can allow a drone to incorporate drag forces into its motion and navigation [3], [6] and, importantly, improve stability [7], [8].

A measurement challenge arises when both airflow signals are present; the flow signal caused by drone motion cannot be easily distinguished from the flow signal caused by wind. No published sensor has been shown to distinguish and interpret flow from two sources simultaneously. This gap contrasts with the natural world, where animals interpret complex flow signals during flight or while swimming using arrays of whisker/hair sensors [9], [10], [11], [12]. For animals such as the harbor seal, an array of whiskers is critical to interpreting the vortices caused by prey while the seal is swimming. As a vortex passes the seal’s upstream whiskers, the whiskers’ shape amplifies the vortices that are then detected by the downstream whiskers [12].

\*This work was supported by MURI award number FA9550-19-1-0386

\*Corresponding Author: Teresa Kent [tkent@andrew.cmu.edu](mailto:tkent@andrew.cmu.edu)

<sup>1</sup> Robotics Institute, Carnegie Mellon University, 5000 Forbes Ave, Pittsburgh, PA, USA

<sup>2</sup> Mechanical Engineering at Carnegie Mellon University, Pittsburgh PA, USA

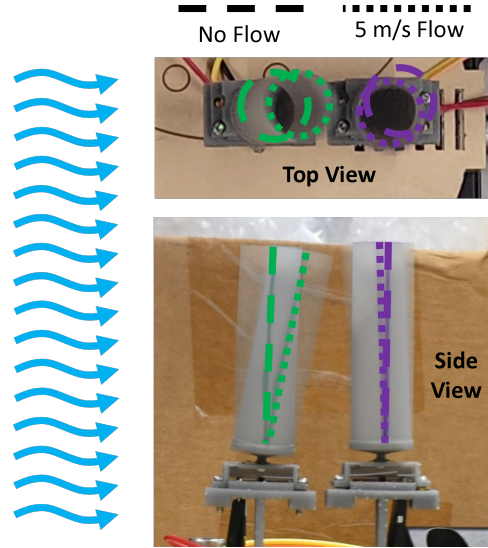


Fig. 1. Top and side views of two whisker-inspired flow sensors demonstrating flow shadowing. The upstream whisker (green) rotates significantly in response to an incident flow. In contrast, the downstream whisker (purple) in the shadow of the upstream whisker oscillates around its original position.

Using the idea that the shape of an array can modify flow across an array, we engineered a sensing array with the novel ability to isolate the distinct headings of two separate flow sources. In our array, upstream whisker-inspired sensors can block or partially block the flow to downstream whiskers, a phenomenon we call “flow shadowing”. In flow shadowing, the upstream whisker(s) receive the full effect of the airflow, but the downstream whisker(s) (which are in the front whisker’s “shadow”) only receive a portion of the flow (Fig. 1). The shadowing becomes multi-directional when a second flow source is introduced, increasing the asymmetry in signal response. Comparing the response of all whiskers in the array allows us to identify the origin heading of two simultaneous flows.

Our first experiment quantifies the flow shadowing phenomenon using a modified version of two previously developed sensors [4], [13] under partial and complete occlusion. We found a linear response between the percent of whisker shadowed and the magnitude of the comparative signal responses. The linear relationship exists in ideal conditions (wind tunnel) and imperfect flow (box fan). Importantly, we determined that reduced spacing between the two whiskers increased the magnitude of the flow shadowing phenomenon under imperfect flow. In our second experiment, we subjected a 2x2 array of whiskers to flow from one or two different

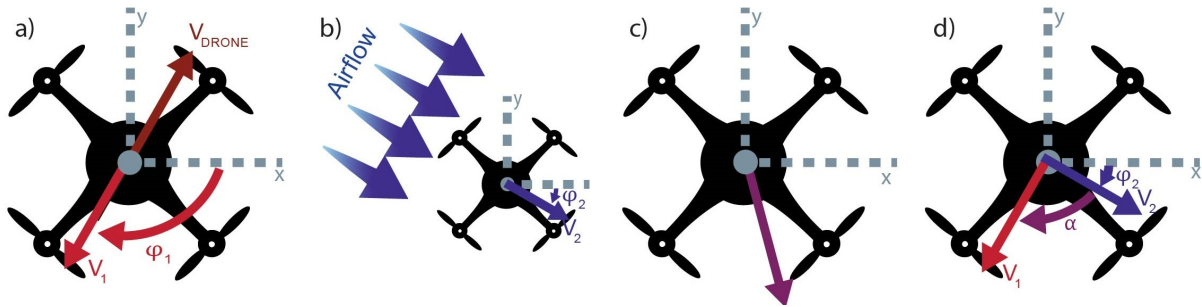


Fig. 2. Diagram of nomenclature for two flow signals. a) Flow 1: A drone flying at velocity  $v_{Drone}$  with a flow sensor onboard measures a flow signal equal to but opposite the drone's velocity ( $v_1, \varphi_1$ ). b) Flow 2: The environment in which a drone flies has wind. An onboard flow sensor will respond to the wind flow ( $v_2, \varphi_2$ ). c) A flow sensor that responds to both flow types equally will measure a combined signal. d)  $\alpha$  is a measure of the difference between the headings of the two flow stimuli ( $\varphi_1$  or  $\varphi_2$ ) which are estimated from an array of flow sensors.

sources, showing that shadowing in multiple directions yields a predictable asymmetric response in an array. We use these asymmetric signals to estimate the flow headings under two conditions: 1) we know the heading of one of the flows, and 2) we have no prior information about the flows.

## II. RELATED WORK

### A. Arrays of hair sensors in biology

Flow-sensing hairs are often critical to aerial flight, giving animals information about speed and stability. One study showed that when hairs were removed from bat wings, the bats altered their flight, performing more naturally stable maneuvers and flying faster [9]. Locusts also use hairs to detect flow and for flight stability. Airflow across locust hairs induces flight movements, which does not occur when their hairs are temporarily desensitized. Hair desensitization also prevents the locust from maintaining stable flight [10].

Most animals that use whiskers/hairs to sense flow use an array of hairs. Understanding the importance of the array neurologically is complex, so much of the prior research on arrays has focused on the array mechanics. Research shows flow-sensing hairs can work together to provide a complete picture of the flow. For example, each of the flow-sensing hairs on a locust responds most strongly to flow from a single direction, but locusts are covered in hairs with different orientations, allowing them to better understand the flow environment [11]. Harbor seals also have whisker arrays. In harbor seals, the upstream whiskers maximize the vortex-induced vibrations caused by their prey to increase the sensing ability of the downstream whiskers [12].

### B. Direct Flow Sensors

There is a long history of 1D flow sensing on commercial aircraft, but here we focus on 2D and 3D flow sensing as it is more relevant to drone flight. Four types of flow sensors have been used to capture both the direction and magnitude of airflows: anemometer arrays [14], [15], [16], [17], [18], pitot tube pressure arrays [19], [20], hot wire arrays [21], [22], [23], [1], and whisker-inspired sensors [4]. The first three sensors (all but the whisker-inspired sensors) use an array of 1D sensors to obtain a 2D or 3D flow vector. Our work

is based on the whisker-inspired sensor; the functionality of this sensor is described in the Methods section.

Previously published flow sensors have demonstrated the benefits of drone velocity sensing [4], [20], [15]. The authors compared the drone velocity estimated from flow sensors to the drone's velocity profile collected from motion tracking data [4], [20]. Good velocity estimation is important for state estimation and navigation tasks. Accurate velocity estimates are also essential for advanced maneuvers, where measurements can help predict lift and drag [5]. All prior demonstrations of velocity estimation via flow were performed in a drone cage with negligible wind.

Information about wind flow provides force information to a drone's flight controller. In [1] and [2], researchers incorporated the flow sensor signal into the drone control algorithm to maintain position stability in gusty flow. In [3], researchers combined flow sensor and IMU data to estimate the direction of an external gust while subtracting flow from motion. The same researchers later showed in simulation how the flow sensor could help a drone land in gusty conditions [7]. In all three papers, the gust represented a significantly larger magnitude flow than any flow due to the drone's motion in contrast to the study presented in our current work.

### C. Indirect Measures of Flow

While the sensors discussed in the prior section measure flow directly, drone velocity, wind [24], and drag [25] have also been measured through indirect measurements. The challenge, similar to direct flow measurements, is that another sensor type must be present to measure multiple flow sources [26]. Optical flow sensors estimate the velocity of a drone by tracking features on earth during the drone's flight [27], [28] provided the environment has sufficiently distinct features. Inertial measurement units (IMUs) have been used to both calculate drone velocity [29] and external wind [26]. Often, data from IMU sensors, GPS and optical flow [30], [31] are fused together to predict velocity, as each one is situationally imperfect at measuring velocity.

### III. METHODS

#### A. Nomenclature

The sensing array aims to define the origin of two flow sources of similar velocity ( $v$ ). The headings of the two flows are labeled  $\varphi_1$  and  $\varphi_2$  relative to the drone. In experimental results,  $\alpha$ , the smallest angle between the two flows is also calculated because differentiating two separate flows becomes more difficult as  $\alpha$  gets smaller. We also expect that the relative magnitudes of the two flows,  $\frac{v_1}{v_2}$ , will also affect our ability to accurately distinguish multiple flow sources. These variables are depicted in Fig. 2.

#### B. Array Manufacturing

The design of the sensing system is the same as [32], [13] and is modeled using the same methods as [13], [32]. The only update is a change in fin shape from a cross [32] to a 50 mm tall, 15 mm diameter hollow cylinder. The cylinder is expected to have a uniform drag response for various flow directions in 2D, which was not true for the cross shape [3].

A diagrammatic representation of the sensor design is in Fig. 3c. A 2 mm<sup>3</sup> magnet (C0020, Supermagnetman) is glued on the backside of a laser-cut spring (photolaser U4, LPKF) made from 0.1 mm steel. A hollow cylinder with a taper at the base is 3D printed using a Formlabs printer and attached to the spring opposite the magnet. As the flow hits the cylinder surface, the cylinder “whisker” rotates about its fixed point (the center of the spring) (Supplementary Video). The magnet also rotates through an equal and opposite angle. A Hall effect sensor (TLE493-W2B6 A0, Infineon) detects this rotation. The magnet and Hall effect sensor are kept at a constant separation by a 3D-printed housing.

The array of sensors (Fig. 3b) maintains a spacing,  $s$ , between whiskers of 35 mm unless explicitly specified otherwise. The spacing is maintained using laser cut and 3D-printed housings and secured with screws. Each sensor in the array is connected to an Arduino Uno through a multiplexer (TCA9548A 1-to-8 I2C Multiplexer) which can sample all four sensors in the array at over 100 Hz.

#### C. Data Processing

When flow hits a whisker, the whisker oscillates about a point where the spring forces and the drag forces are balanced [32] (Supplementary Video). The average rotation magnitude and direction are indicative of the velocity and direction of flow. These features of rotation are measured by changes in the magnetic field signal recorded by the 3 axes of the Hall effect sensor ( $B_{xn}$ ,  $B_{yn}$  and  $B_{zn}$ ). The Hall effect sensors’ axes are aligned with the axis of the full array (Fig. 3a) and the numbers circled in Fig. 3b represent the whisker number in the array.

To counteract variability in the manufacturing process, each sensor is calibrated individually by applying a 5.5 m s<sup>-1</sup> flow parallel to the Hall effects sensor’s +x, -x, +y, and -y axes in turn. These stored values can be used to normalize the response to analyze data. After calibrating the sensor, the magnetic field signals  $B_{xn}$  and  $B_{yn}$  are passed through an averaging filter with a window of 5 before solving for

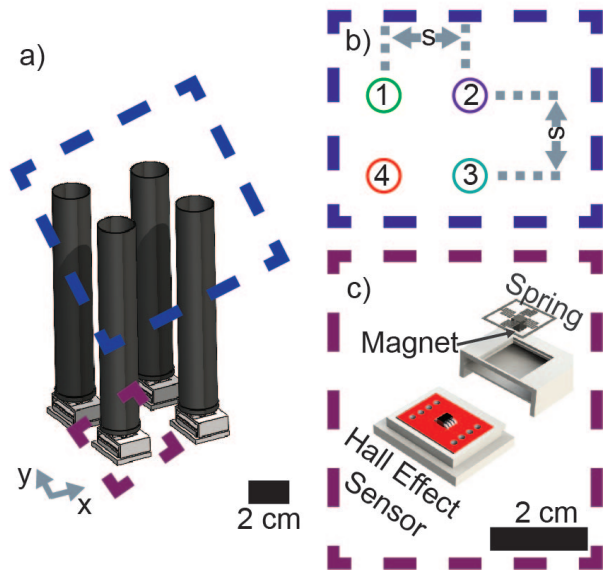


Fig. 3. a) 2x2 array design. b) Four whiskers are separated by  $s = 35$  mm in both x and y axes in an array. c) The sensors are designed similar to [32]. A Hall effect sensor measures the rotations of the whisker drag element suspended by a spring. (Supplementary Video).

the magnitude of the signal ( $\|B_n\|_2$ ). Subscript  $n$  refers to the sensor number in the array. Averaging is important as it allows us to solve for the net vector rather than the magnitude of oscillation. Finally we solve for the direction of each sensor’s signal ( $\theta_n$ ).  $\theta_n$  is always a measurement of an individual sensor and  $\varphi$  (Fig. 2) is always a prediction about environmental flow.

$$\theta_n = \arctan \frac{B_{yn}}{B_{xn}} \quad (1)$$

$$\|B_n\|_2 = \sqrt{B_{xn}^2 + B_{yn}^2} \quad (2)$$

When measuring flow shadowing, the final step is to normalize the signal magnitude by  $\|B_{max}\|_2$ , the max value of  $\|B_n\|_2$  in the array. This step provides a magnitude relative to the array rather than relative to the calibration velocity.

#### D. Experimental Setups

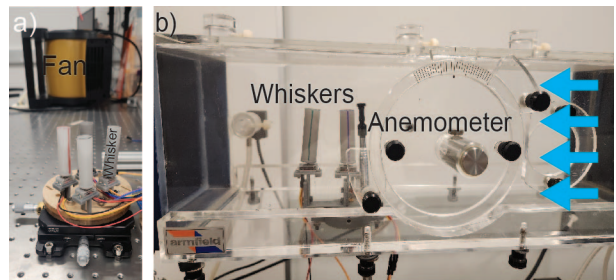


Fig. 4. The whisker arrays were tested under two types of airflow. a) One or two fans supplied airflow to a whisker array mounted on an optical table. The optical table and a ThorLabs rotational stage aided repeatability as the headings of flow were varied around the array. b) A wind tunnel was used to apply airflow from a single direction to whisker arrays.

1) *Wind Tunnel Tests*: Wind tunnel tests (Fig. 4b) were carried out in a C15-10 Armfield subsonic wind tunnel. An anemometer (4330, Thomas Scientific) was placed next to the sensing array to ensure that the desired velocities were reached. The mounts for the tests were 3D printed to allow flow orientation to be controlled at intervals of  $5^\circ$ . Wind tunnel tests were used to evaluate the response of pairs of sensors to flow from a single direction.

2) *Box Fan Testing*: Multiple flow directions cannot be provided in a controlled wind tunnel setup, so instead two box fans (Lasko Pro performance three-speed fan, Stanley Model 655 704 three-speed fan) were used to evaluate flow from multiple sources (Fig. 4a). The second fan was only used to test flow from multiple sources, and we made no attempt to keep these flows laminar. Here, the array was placed on a Thorlabs manual stage which allowed for control of the incident angle of flow within  $0.5^\circ$  relative to the array. Fan tests were used to evaluate the response of individual sensors, pairs of sensors, and a  $2 \times 2$  array of sensors to flow from one or more sources.

### E. Experimental Tests

1) *Sensor Characterization*: Using the box fan setup, a single whisker was tested under single flow with orientations between  $0^\circ$ - $360^\circ$  in increments of  $10^\circ$ . The test was performed at  $6.5 \text{ m s}^{-1}$ .

2) *Flow Shadowing*: We characterized flow shadowing with pairs of whiskers using both the box fan and wind tunnel environments. Using both environments allowed us to determine how whisker sensor responses could be affected by the additional turbulence applied by the fans. Two whiskers were separated by a spacing  $s = (35 \text{ mm in the wind tunnel } 30 \text{ mm using the fan})$ . The whiskers were rotated around the upstream whisker in headings ( $\varphi$ ) of five degree increments between  $-30^\circ$  and  $30^\circ$ . The variation in heading angle changed the percent of occlusion ( $\%_{occ}$ ) of the downstream whisker which was calculated as follows, where  $d$  represents the diameter of the drag element.

$$\%_{occ} = \frac{d - \min\{s * \sin(\varphi), d\}}{d} \quad (3)$$

In the wind tunnel, flow velocities of both  $5 \text{ m s}^{-1}$  and  $6.5 \text{ m s}^{-1}$  were applied to the sensors. For the box fans, velocities of  $5.5 \text{ m s}^{-1}$  and  $6.5 \text{ m s}^{-1}$  were applied. First the signals were normalized compared to the values recorded during the calibration data. Second we solved for  $\theta_n$  and  $\|B_n\|_2$  using Eqns. 1,2. Finally, the value of the upstream and the downstream whiskers were compared to calculate  $\frac{\|B_{down}\|_2}{\|B_{up}\|_2}$ , where ‘up’ represents the signal from the upstream whisker, e.g., the whisker closer to the fan. The tests were repeated, switching the upstream and downstream whiskers.

3) *Spacing Tests*: We also tested how the spacing between a pair of whiskers,  $s$ , affected the amount of flow shadowing under 100% occlusion (Eqn. 3, the upstream whisker completely shadowing the downstream whisker) using the fan experiment.  $s$  was varied from 30 mm to 50 mm in 5 mm increments (Fig. 4a). The applied flow speed was  $6.5 \text{ m s}^{-1}$ .

In initial tests, we found that the two whiskers made contact at this flow speed if the spacing was below 30 mm.

4) *Single and Double Flow Characterization*: We tested how the measured response of a  $2 \times 2$  array of four whiskers (Fig. 4a) varied under different headings and velocities of airflow. The array was tested in all combinations of the following variables  $\varphi_1 = \{0^\circ, 15^\circ\}$ ,  $\alpha = \{45^\circ, 90^\circ, 135^\circ\}$ ,  $v_1 = \{5.2, 6.5 \text{ m s}^{-1}\}$  and  $v_2 = \{7.3, 8.3 \text{ m s}^{-1}\}$ . Combinations of the flow speeds led to  $\frac{v_1}{v_2}$  ratios of  $\{0.60, 0.71, 0.90\}$ .

### F. Algorithm

Two algorithms were considered in this work. In Method 1, we assume that  $\varphi_1$  is known (e.g., from an IMU or optic flow sensor) and we use the array results to solve for  $\varphi_2$ . In Method 2, we assume that no information is known about either  $\varphi$  and solve for both headings. The magnitude and angle from each whisker sensor is combined into a vector  $\vec{B}_n$ . The two methods are outlined below, but are also visually represented in Fig. 10.

#### Method 1: $\varphi_1$ is known

- 1) Using Eqns. 3, 4 predict the expected response of Flow 1,  $\vec{B}'_n$ , with known  $\varphi_1$ .
- 2)  $\Delta \vec{B}_n = \vec{B}_n - \vec{B}'_n$
- 3) Remove whisker data where  $\%_{occ} = 0$ .
- 4) Decompose  $\Delta \vec{B}_n$  into  $\Delta B_y$  and  $\Delta B_x$ .
- 5) predicted  $\varphi_2 = \arctan\left(\frac{\sum_{i=1}^n \Delta B_y}{\sum_{i=1}^n \Delta B_x}\right)$

#### Method 2: Solving for both $\varphi$ values

- 1) Estimate  $\varphi_1$ : A first estimate for  $\varphi_1$  can be found from the  $\theta_n$  value furthest from the mean of all  $\theta_n$ ,  $\hat{\theta}$ . Picking this value decreases the chance of predicting  $\varphi_1$  as the net flow.
- 2) Using Eqns. 3, 4 predict the expected response of first flow,  $\vec{B}'_n$ , with predicted  $\varphi_1$ .
- 3)  $\Delta \vec{B}_n = \vec{B}_n - \vec{B}'_n$
- 4) Decompose  $\Delta \vec{B}_n$  into  $\Delta B_y$  and  $\Delta B_x$
- 5) predicted  $\varphi_2 = \arctan\left(\frac{\sum_{i=1}^n \Delta B_y}{\sum_{i=1}^n \Delta B_x}\right)$
- 6) Repeat steps 2-5, starting with  $\varphi_2$  as the input flow to improve upon  $\varphi_1$  prediction.

## IV. RESULTS AND DISCUSSION

### A. Single Sensor Characterization

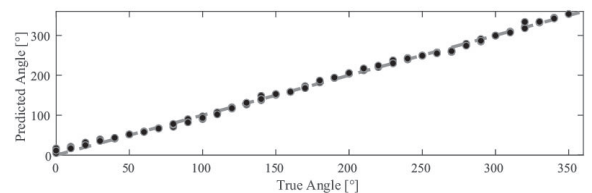


Fig. 5. Comparison of the true heading of flow ( $\varphi$ ) versus the sensor predicted flow heading ( $\theta$ ) for a single sensor with airflow provided by a fan. Each heading includes two trials.

The sensor was updated from [32] to obtain a uniform response from all flow headings by changing the previous cross shape to a circle. The accuracy of the sensor’s  $\theta$  reading was compared to the applied flow  $\varphi$  and found to be accurate with a root mean square error of  $5.22^\circ$  (Fig. 5).

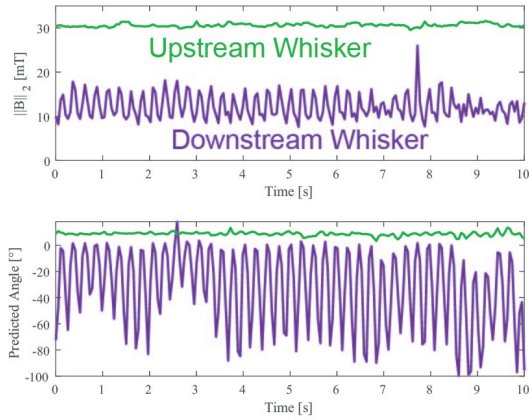


Fig. 6. Results from a single trial of two whiskers placed under a flow of  $v = 6.5 \text{ m s}^{-1}$ ,  $\varphi = 0^\circ$  in the wind tunnel. In this case,  $\%_{occ} = 100\%$ . a) Magnitude of the upstream (green) and downstream (purple) whisker response ( $\|B\|_2$ , Eqn. 2). b) The estimated direction of the whiskers' responses ( $\theta$ , Eqn. 1).

### B. Flow Shadowing Characterization

Two sensor arrays were used to characterize flow shadowing. As expected (and seen in Figs. 1 and 6), the downstream whisker exhibits a smaller signal response  $\|B_{down}\|$  when occluded by the upstream whisker. Results in Fig. 6 also indicate that a more turbulent flow is incident on the downstream whisker. The  $\|B_{down}\|$  signal is more oscillatory and the predicted angle changes frequently. These results were true in both the wind tunnel and under flow from the box fan although the oscillations of both whiskers were greater under the more turbulent flow from the box fan.

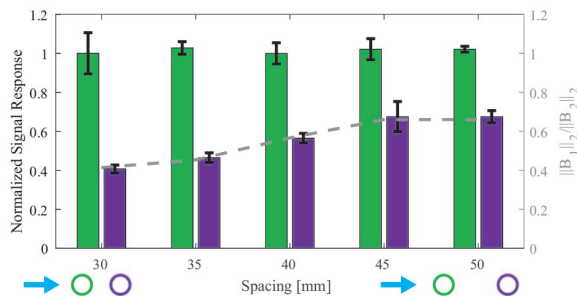


Fig. 7. The signal response of two whiskers under 100% occlusion were recorded as the spacing,  $s$ , between the two whiskers was changed.

1) *Spacing*: We predicted that the effect of flow shadowing would decrease as the spacing between the whiskers increased. This expectation agreed with the results in Fig. 7. The results indicated that a more densely packed array of whiskers will improve the flow shadowing effect. We chose a final spacing of 35 mm to maximize flow shadowing while minimizing the chance of whisker-to-whisker contact.

2) *Percent Occlusion*: Fig. 8 compares the relative magnitudes of the upstream and downstream whiskers versus the expected percent of occlusion (Eqn. 3). Note that in the results, some flow reaches the downstream whisker even

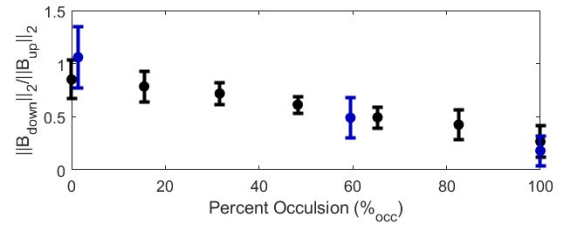


Fig. 8. Whisker sensors were rotated relative to each other and the heading of flow. This rotation changed  $\%_{occ}$  as calculated in Eqn. 3. When  $\%_{occ} \approx 100\%$  the downstream whisker's surface area is fully shadowed by the upstream whisker. When  $\%_{occ} \approx 0\%$  the downstream whisker is fully exposed to the flow. The affect of this shadowing on the sensor signal was measured using the fan and wind tunnel setups. The tests were performed with a fan (black) and then repeated in a wind tunnel (blue). The spacing in the fan test was 30 mm and in the wind tunnel 35 mm

at 100% occlusion. Flow occlusion was tested in a variety of wind flow types and directions of the whisker; in every result a linear trend was the best descriptor between the percent occlusion and the magnitude ratio. For the algorithm portion of the study, this relationship is represented with the following equation.

$$\frac{\|B_{down}\|_2}{\|B_{up}\|_2} = 1 - 0.8 * (\%_{occ}/100) \quad (4)$$

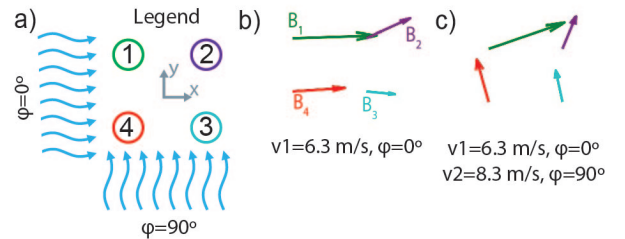


Fig. 9. Visualization of the flow vectors from the 2x2 array of whiskers in a) under b) one and c) two sources of flow.

### C. Single and Double Flow Characterization

The effect of occlusion is also seen on a 2x2 array of four whiskers under single flow (Fig. 9b). In the example shown, the upstream whiskers' magnitude response  $\|B\|_2$  is larger than the downstream whiskers. The flow direction predicted by the upstream whiskers ( $\theta$ ) is also more accurate to the true flow heading ( $\varphi_1 = 0^\circ$ ). When a second flow source is introduced (Fig. 9c), flow blocking becomes multi-directional. In this experiment, whisker 1 is 100% occluded from the second flow source at  $\varphi_2 = 90^\circ$  and therefore the majority of its magnetic field response ( $B$ ) is due to flow 1 ( $\varphi_1 = 0^\circ$ ). In contrast, whiskers 3 and 4 are 0% occluded from the  $90^\circ$  flow which is also a higher velocity flow than flow 1 so their signal is strongly affected by flow 2. Whisker 2 is 100% occluded from both sources of flow and its direction prediction is closer to the net flow that we would expect if no flow shadowing occurred. The flow shadowing responses in Fig. 9c illustrate the asymmetry in the whisker response across the array that allows us to estimate headings

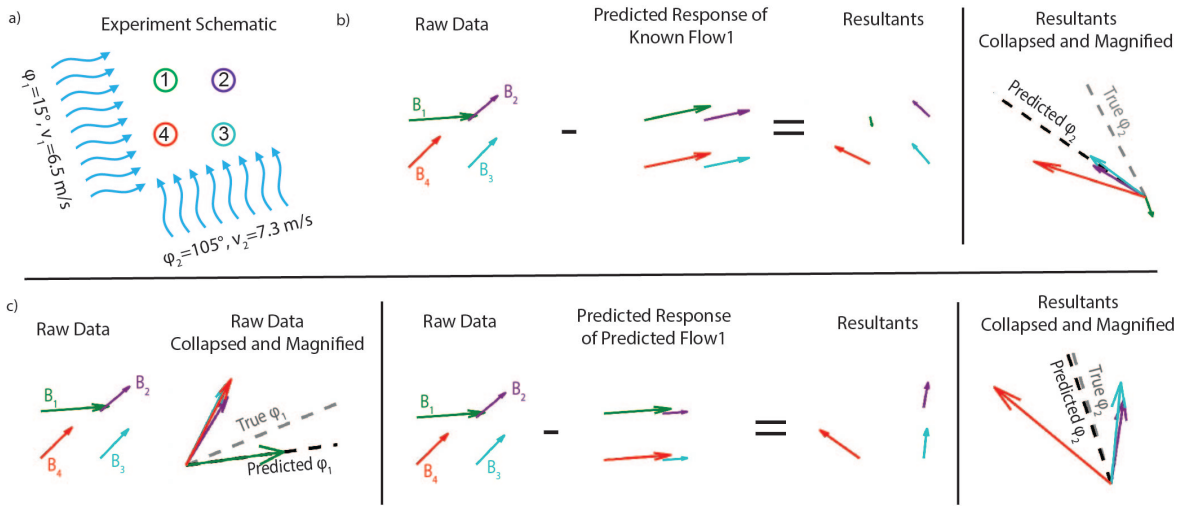


Fig. 10. a) A single trial of data is used to illustrate how the two algorithms work. b) Algorithm 1 considers a scenario where one of the directions of flow is known ( $\varphi_1$ ) and the algorithm needs to estimate  $\varphi_2$ . c) Algorithm 2 is designed to estimate  $\varphi_1$  and  $\varphi_2$  with no prior knowledge. It therefore begins by making a guess about  $\varphi_1$  before applying a similar method to Algorithm 1.

of the two flow sources and prevents the problem shown in (Fig. 2c) where all four sensors respond to the average flow.

#### D. Algorithm

The algorithms to estimate  $\varphi_2$  (if  $\varphi_1$  is known) or  $\varphi_{1,2}$  (if no flows are known) take advantage of the array's asymmetry. Method 1 uses the known  $\varphi_1$ , calculates the expected flow across the array for this flow from Eqn. 4, and uses the result to estimate the direction of the second flow (Fig. 10b). Method 2 assumes no prior knowledge of the flow headings. A first estimate of  $\varphi_1$  is found from the flow direction in the array most separate from the mean (Fig. 10c).  $\varphi_2$  is then estimated using a similar approach to Method 1.

Results were collected across at least 2 trials of 24 different combinations of two flows with varying headings and speeds and are summarized in Table I for angle combinations with  $\alpha = 90^\circ$  and  $135^\circ$ . For each  $\alpha$  and flow speed ratio, a root mean square error (RMSE) was calculated for all trials as  $RMSE = \sqrt{\sum_1^n (\varphi_x - \varphi_{x,predicted})^2 / n}$ .

TABLE I  
FLOW HEADING RMSE ACROSS ALL TRIALS

$\alpha$	$\frac{v_1}{v_2}$	Method 1		Method 2	
		$\varphi_2$ RMSE	$\varphi_1$ RMSE	$\varphi_1$ RMSE	$\varphi_2$ RMSE
$90^\circ$	0.9	$30.5^\circ$	$9.9^\circ$	$22.9^\circ$	$22.9^\circ$
$90^\circ$	0.7	$16.0^\circ$	$13.2^\circ$	$23.7^\circ$	$23.7^\circ$
$90^\circ$	0.6	$15.4^\circ$	$7.8^\circ$	$7.3^\circ$	$7.3^\circ$
$135^\circ$	0.9	$8.9^\circ$	$43.2^\circ$	$26.1^\circ$	$26.1^\circ$
$135^\circ$	0.7	$22.1^\circ$	$36.3^\circ$	$24.9^\circ$	$24.9^\circ$
$135^\circ$	0.6	$20.2^\circ$	$45.0^\circ$	$16.8^\circ$	$16.8^\circ$

Overall, the calculated RMSE for the various headings across both algorithms were relatively low, especially given that a small array of whiskers (2x2) was used in this study. We did find in test cases when  $\alpha = 45^\circ$  (not included in Table I) that error became significantly higher. In these cases where the two incident flow sources are closer in direction, the small 2x2 array is not able to provide enough asymmetry. The

creation of larger arrays to improve accuracy and the smallest distinguishable  $\alpha$  is an interesting direction for future study. The velocity ratio also seems to affect the accuracy of the heading predictions although we cannot yet say this with statistical certainty. As expected, prediction estimates seem to improve as the velocity ratio moves further away from 1 (e.g., one flow is significantly faster than the other). Finally, while the results presented are calculated from 50 collected data points, the algorithms will work with as few as 5 data points since these result in a standard deviation below the sensor's RMSE. This will ultimately reduce the time required to estimate the flow vectors.

#### V. CONCLUSION

This work demonstrates the benefits of flow shadowing, a phenomenon that occurs when whiskers are packed densely in an array, for estimating the headings of multiple flow sources. Using a modified version of whisker-based flow sensors from previous work [4], we quantified the flow shadowing effect and derived an empirical model. Using a 2x2 whisker array, we showed that flow shadowing creates a direction-dependent asymmetric response. Asymmetry in the array response allowed our algorithms to predict the flow headings with relative accuracy. We expect that more whiskers, a higher density, and improvements to the algorithm can further improve our results, including an estimate of velocity for both flows. The work presented here represents the first steps toward sensors that are capable of a more nuanced understanding of the flow surrounding a variety of unmanned aerial vehicles.

#### ACKNOWLEDGEMENTS

This research effort was supported by Air Force Office of Scientific Research MURI award number FA9550-19-1-0386. The authors would also like to thank Prof. Satbir Singh and Mr. Ed Wojciechowski for the instruction and guidance in use of the wind tunnel characterization facility.

## REFERENCES

- [1] N. Simon, A. Z. Ren, A. Piqué, D. Snyder, D. Barretto, M. Hultmark, and A. Majumdar, "Flowdrone: wind estimation and gust rejection on uavs using fast-response hot-wire flow sensors," *arXiv preprint arXiv:2210.05857*, 2022.
- [2] C. Wang, S. Wang, G. De Croon, and S. Hamaza, "Embodied airflow sensing for improved in-gust flight of flapping wing mavs," *Frontiers in Robotics and AI*, p. 338, 2022.
- [3] A. Tagliabue, A. Paris, S. Kim, R. Kubicek, S. Bergbreiter, and J. P. How, "Touch the wind: Simultaneous airflow, drag and interaction sensing on a multirotor," *arXiv preprint arXiv:2003.02305*, 2020.
- [4] S. Kim, R. Kubicek, A. Paris, A. Tagliabue, J. P. How, and S. Bergbreiter, "A whisker-inspired fin sensor for multi-directional airflow sensing," *IROS*, 2020.
- [5] S. B. Fuller, M. Karpelson, A. Censi, K. Y. Ma, and R. J. Wood, "Controlling free flight of a robotic fly using an onboard vision sensor inspired by insect ocelli," *Journal of The Royal Society Interface*, vol. 11, no. 97, p. 20140281, 2014.
- [6] A. Tagliabue and J. P. How, "Airflow-inertial odometry for resilient state estimation on multirotors," in *2021 IEEE International Conference on Robotics and Automation (ICRA)*. IEEE, 2021, pp. 5736–5743.
- [7] A. Paris, A. Tagliabue, and J. P. How, "Autonomous mav landing on a moving platform with estimation of unknown turbulent wind conditions," in *AIAA Scitech 2021 Forum*, 2021, p. 0378.
- [8] S. Fuller, Z. Yu, and Y. P. Talwekar, "A gyroscope-free visual-inertial flight control and wind sensing system for 10-mg robots," *Science Robotics*, vol. 7, no. 72, p. eabq8184, 2022.
- [9] S. Sterbing-D'Angelo, M. Chadha, C. Chiu, B. Falk, W. Xian, J. Barcelo, J. M. Zook, and C. F. Moss, "Bat wing sensors support flight control," *Proceedings of the National Academy of Sciences*, vol. 108, no. 27, pp. 11 291–11 296, 2011.
- [10] B. L. Boubilil, C. A. Diebold, and C. F. Moss, "Mechanosensory hairs and hair-like structures in the animal kingdom: specializations and shared functions serve to inspire technology applications," *Sensors*, vol. 21, no. 19, p. 6375, 2021.
- [11] J. M. Camhi, "Locust wind receptors: I. transducer mechanics and sensory response," *Journal of Experimental Biology*, vol. 50, no. 2, pp. 335–348, 1969.
- [12] X. Zheng, A. M. Kamat, M. Cao, and A. G. P. Kottapalli, "Wavy whiskers in wakes: Explaining the trail-tracking capabilities of whisker arrays on seal muzzles," *Advanced Science*, vol. 10, no. 2, p. 2203062, 2023.
- [13] T. Wang, T. A. Kent, and S. Bergbreiter, "Design of whisker-inspired sensors for multi-directional hydrodynamic sensing," 2023.
- [14] N. N. Minh-Dung, H. Takahashi, K. Kuwana, T. Takahata, K. Matsumoto, and I. Shimoyama, "3d airflow velocity vector sensor," in *2011 IEEE 24th International Conference on Micro Electro Mechanical Systems*. IEEE, 2011, pp. 513–516.
- [15] P. Bruschi, M. Piotto, F. Dell'Agnello, J. Ware, and N. Roy, "Wind speed and direction detection by means of solid-state anemometers embedded on small quadcopters," *Procedia Engineering*, vol. 168, pp. 802–805, 2016.
- [16] C. Liu, L. Du, Z. Zhao, Z. Fang, and L. Li, "A directional anemometer based on mems differential pressure sensors," in *The 9th IEEE International Conference on Nano/Micro Engineered and Molecular Systems (NEMS)*. IEEE, 2014, pp. 517–520.
- [17] E. Arens, A. Ghahramani, R. Przybyla, M. Andersen, S. Min, T. Peffer, P. Raftery, M. Zhu, V. Luu, and H. Zhang, "Measuring 3d indoor air velocity via an inexpensive low-power ultrasonic anemometer," *Energy and Buildings*, vol. 211, p. 109805, 2020.
- [18] M. Piotto, G. Pennelli, and P. Bruschi, "Fabrication and characterization of a directional anemometer based on a single chip mems flow sensor," *Microelectronic Engineering*, vol. 88, no. 8, pp. 2214–2217, 2011.
- [19] P. Bruschi, M. Dei, and M. Piotto, "A low-power 2-d wind sensor based on integrated flow meters," *IEEE Sensors Journal*, vol. 9, no. 12, pp. 1688–1696, 2009.
- [20] K. Haneda, K. Matsudaira, R. Noda, T. Nakata, S. Suzuki, H. Liu, and H. Takahashi, "Compact sphere-shaped airflow vector sensor based on mems differential pressure sensors," *Sensors*, vol. 22, no. 3, p. 1087, 2022.
- [21] J. A. Defay, J. M. Peters, and K. H. Petersen, "A customizable, low-cost alternative for distributed 2d flow sensing in swarms," *Artificial Life and Robotics*, vol. 27, no. 2, pp. 272–277, 2022.
- [22] Y. Ye, Z. Yi, S. Gao, M. Qin, and Q.-A. Huang, "Octagon-shaped 2-d micromachined thermal wind sensor for high-accurate applications," *Journal of Microelectromechanical Systems*, vol. 27, no. 4, pp. 739–747, 2018.
- [23] S. Gao, Z. Yi, Y. Ye, M. Qin, and Q.-A. Huang, "Configuration of a self-heated double wheatstone bridge for 2-d wind sensors," *Journal of Microelectromechanical Systems*, vol. 28, no. 1, pp. 125–130, 2018.
- [24] T. Tomić, *Model-based control of flying robots for robust interaction under wind influence*. Springer Nature, 2022, vol. 151.
- [25] J. Jia, K. Guo, X. Yu, W. Zhao, and L. Guo, "Accurate high-maneuvering trajectory tracking for quadrotors: A drag utilization method," *IEEE Robotics and Automation Letters*, vol. 7, no. 3, pp. 6966–6973, 2022.
- [26] P. P. Neumann and M. Bartholmai, "Real-time wind estimation on a micro unmanned aerial vehicle using its inertial measurement unit," *Sensors and Actuators A: Physical*, vol. 235, pp. 300–310, 2015.
- [27] W. Ding, J. Wang, S. Han, A. Almagbile, M. A. Garratt, A. Lambert, and J. J. Wang, "Adding optical flow into the gps/ins integration for uav navigation," in *Proc. of International Global Navigation Satellite Systems Society Symposium*. Citeseer, 2009, pp. 1–13.
- [28] H. Chao, Y. Gu, and M. Napolitano, "A survey of optical flow techniques for robotics navigation applications," *Journal of Intelligent & Robotic Systems*, vol. 73, pp. 361–372, 2014.
- [29] M. F. Sani and G. Karimian, "Automatic navigation and landing of an indoor ar. drone quadrotor using aruco marker and inertial sensors," in *2017 international conference on computer and drone applications (IConDA)*. IEEE, 2017, pp. 102–107.
- [30] P.-J. Bristeau, F. Callou, D. Vissière, and N. Petit, "The navigation and control technology inside the ar. drone micro uav," *IFAC Proceedings Volumes*, vol. 44, no. 1, pp. 1477–1484, 2011.
- [31] J. Engel, J. Sturm, and D. Cremers, "Accurate figure flying with a quadcopter using onboard visual and inertial sensing," *Imu*, vol. 320, no. 240, 2012.
- [32] S. Kim, C. Velez, D. K. Patel, and S. Bergbreiter, "A magnetically transduced whisker for angular displacement and moment sensing," *IEEE/RSJ International Conference on Intelligent Robots and Systems (IROS)*, 2019.